displayed the same intracellular localization as wild-type Rhes. Biochemical studies revealed a substantial reduction of Rhes-C263S binding to Ubc9 and mHtt (Fig. 4D). Finally, Rhes-induced mHtt sumoylation occurred both in the soluble and membrane fractions (fig. S9).

In summary, Rhes binds to mHtt and elicits its sumoylation, which is associated with mHtt disaggregation and cell death. In some animal models overexpression of full-length mHtt augments aggregates in the striatum (20, 21), although, in other models, the overexpression leads to fewer or no aggregates (22, 23). In human HD patients and several animal models, aggregates are not correlated with cell death (5, 20, 24–26). Sumoylated mHtt represses nuclear transcription (8). We observed caspase-3 activation in Rhes-mHtt cells, and mHtt is known to induce cytochrome c release (27).

Rhes elicits sumoylation of mHtt via a mechanism independent of its GTPase activity but which does require cysteine at CXXX domains presumably for farnesylation and membrane attachment. Sumoylation of mHtt, RanGAP1, and SP100 occurs in the absence of Rhes but is markedly augmented by Rhes. The three well-studied SUMO E3 ligases, the PIASy family, Pc2, and RanBP2, do not share obvious sequence homology with each other (28) or with Rhes, the only G protein with demonstrated E3 ligase activity.

Dexras1, a close homolog of Rhes, displays the highest levels in the brain, but with no marked regional differences (29). Dexras1 mediates linking of nitric oxide (NO) signaling by CAPON, a scaffolding protein, which links Dexras1 to neuronal NO synthase (29). NO serves as a guanine nucleotide–exchange factor to activate Dexras1. Dexras1 also mediates neurotoxic iron influx following glutamate–N-methyl-D-aspartate neurotransmission (30).

Our discovery that the striatal-selective protein Rhes partners with mHtt to elicit cytotoxicity can account for the striatal pathophysiology of HD. Although Rhes is uniquely enriched in the striatum, it displays detectable cerebral cortical levels with negligible values in the cerebellum (9, 31). Cortical damage presumably elicits dementia; however, the cerebellum is relatively impervious to neurotoxic damage. Because HD can be diagnosed many years before the onset of symptoms, prophylactic therapy could, in principle, prevent or delay the onset of symptoms. Drugs that block the binding of Rhes and mHtt may thus have therapeutic potential.

References and Notes
1. J. F. Gusella, M. E. Macdonald, *Trends Biochem. Sci.* **31**, 533 (2006).
2. C. M. Cowan, L. A. Raymond, *Curr. Top. Dev. Biol.* **75**, 25 (2006).
3. K. A. Sieradzan, D. M. Mann, *Neuropathol. Appl. Neurobiol.* **27**, 1 (2001).
4. F. Saudou, S. Finkbeiner, D. Devys, M. E. Greenberg, *Cell* **95**, 55 (1998).
5. S. Kuemmerle et al., *Ann. Neurol.* **46**, 842 (1999).
6. M. Arrasate, S. Mitra, E. S. Schweitzer, M. R. Segal, S. Finkbeiner, *Nature* **431**, 805 (2004).
7. B. Gong, M. C. Lim, J. Wanderer, A. Wyttenbach, A. J. Morton, *Brain Res. Bull.* **75**, 146 (2008).
8. J. S. Steffan et al., *Science* **304**, 100 (2004).
9. J. D. Falk et al., *J. Neurosci. Res.* **57**, 782 (1999).
10. Materials and methods are available as supporting material on *Science* Online.
11. F. Trettel et al., *Hum. Mol. Genet.* **9**, 2799 (2000).
12. G. Schilling et al., *Hum. Mol. Genet.* **8**, 397 (1999).
13. Q. Ruan, M. Lesort, M. E. MacDonald, G. V. Johnson, *Hum. Mol. Genet.* **13**, 669 (2004).
14. Single-letter abbreviations for the amino acid residues are as follows: A, Ala; C, Cys; D, Asp; E, Glu; F, Phe; G, Gly; H, His; I, Ile; K, Lys; L, Leu; M, Met; N, Asn; P, Pro; Q, Gln; R, Arg; S, Ser; T, Thr; V, Val; W, Trp; Y, Tyr; and X, any amino acid.
15. A. Pichler, A. Gast, J. S. Seeler, A. Dejean, F. Melchior, *Cell* **108**, 109 (2002).
16. M. H. Kagey, T. A. Melhuish, D. Wotton, *Cell* **113**, 127 (2003).
17. T. Magee, M. C. Seabra, *Curr. Opin. Cell Biol.* **17**, 190 (2005).
18. P. Vargiu et al., *Oncogene* **23**, 559 (2004).
19. L. P. Wright, M. R. Philips, *J. Lipid Res.* **47**, 883 (2006).
20. V. C. Wheeler et al., *Hum. Mol. Genet.* **9**, 503 (2000).
21. C. H. Lin et al., *Hum. Mol. Genet.* **10**, 137 (2001).
22. P. H. Reddy et al., *Nat. Genet.* **20**, 198 (1998).
23. M. S. Levine et al., *J. Neurosci. Res.* **58**, 515 (1999).
24. J. G. Hodgson et al., *Neuron* **23**, 181 (1999).
25. P. F. Shelbourne, *Hum. Mol. Genet.* **8**, 763 (1999).
26. C. A. Gutekunst, *J. Neurosci.* **19**, 2522 (1999).
27. Y. S. Choo, G. V. Johnson, M. MacDonald, P. J. Detloff, M. Lesort, *Hum. Mol. Genet.* **13**, 1407 (2004).
28. R. Geiss-Friedlander, F. Mechior, *Nat. Rev. Mol. Cell Biol.* **8**, 947 (2007).
29. M. Fang et al., *Neuron* **28**, 183 (2000).
30. J. H. Cheah et al., *Neuron* **51**, 431 (2006).
31. H. Usui et al., *J. Neurosci.* **14**, 4915 (1994).
32. We thank I. Rao, A. Hayashi, K. Ishizuka and M. Chakraborty for technical support. We thank N. Shahani and R. Mealer for critically reading the manuscript. We thank E. Fossale and M. Macdonald for generously providing striatal cell lines. We thank M. Matunis for providing SUMO-related constructs, H. Zoghbi for ataxin constructs, S. Li and X. J.Li for purified Htt, J. Nathans for use of his cell culture facility and Alessandro Usiello for providing antibody to Rhes. Supported by USPHS grant MH18501 and Research Scientist Award DA00074 (SHS).

Mechanoenzymatic Cleavage of the Ultralarge Vascular Protein von Willebrand Factor

Xiaohui Zhang,[1,3]* Kenneth Halvorsen,[2]* Cheng-Zhong Zhang,[1] Wesley P. Wong,[2]† Timothy A. Springer[1]†

Von Willebrand factor (VWF) is secreted as ultralarge multimers that are cleaved in the A2 domain by the metalloprotease ADAMTS13 to give smaller multimers. Cleaved VWF is activated by hydrodynamic forces found in arteriolar bleeding to promote hemostasis, whereas uncleaved VWF is activated at lower, physiologic shear stresses and causes thrombosis. Single-molecule experiments demonstrate that elongational forces in the range experienced by VWF in the vasculature unfold the A2 domain, and only the unfolded A2 domain is cleaved by ADAMTS13. In shear flow, tensile force on a VWF multimer increases with the square of multimer length and is highest at the middle, providing an efficient mechanism for homeostatic regulation of VWF size distribution by force-induced A2 unfolding and cleavage by ADAMTS13, as well as providing a counterbalance for VWF-mediated platelet aggregation.

Von Willebrand factor (VWF) is the key shear-sensing protein in hemostasis and is especially important in arterial bleeding where shear is high (1). VWF is biosynthesized and stored in the Weibel-Palade bodies of endothelial cells in an ultralarge form (ULVWF). The VWF 240,000 M_r monomer (Fig. 1A) is concatenated through specific disulfide bonds at both its N and C termini into multimers of up to ~50 × 10^6 M_r in ULVWF (1, 2). ULVWF is secreted in response to thrombogenic stimuli. A portion of secreted ULVWF is bound locally to endothelial cells from which it is released and also through its A3 domain to collagen at sites of tissue injury. Vessel wall–bound VWF multimers, as well as multimers free in the bloodstream, are extended to a length of up to 15 μm by the hydrodynamic forces in shear flow (2). These forces induce a conformational change in VWF that exposes a binding site in the A1 domain for the platelet glycoprotein Ib (GPIb) molecule, which enables formation of a hemostatic platelet plug (1, 3).

Within 2 hours after release from endothelium into the circulation, ULVWF is converted by ADAMTS13 to smaller multimers with a wide range of size distributions that are characteristic of the circulating pool of VWF (4). Because the length of VWF multimers strongly correlates with

[1]Immune Disease Institute, Harvard Medical School, Boston, MA 02115, USA. [2]Rowland Institute at Harvard, Harvard University, Cambridge, MA 02142, USA. [3]State Key Laboratory of Molecular Biology, Institute of Biochemistry and Cell Biology, Chinese Academy of Sciences, Shanghai 200031, China.

*These authors contributed equally to this work.
†To whom correspondence should be addressed. E-mail: springer@idi.harvard.edu or wong@rowland.harvard.edu

hemostatic potential, cleavage by ADAMTS13 is an important regulatory mechanism. Absence of ADAMTS13 results in increased thrombogenic potential of VWF and thrombotic thrombocytopenic purpura, a life-threatening disease caused by uncontrolled microvascular thrombosis (5). On the other hand, mutations in the A2 domain that presumably destabilize it cause excessive cleavage by ADAMTS13 and a shift in the size distribution to smaller VWF multimers with less hemostatic potential, resulting in the bleeding disorder known as type 2A von Willebrand disease (3, 6).

VWF is cleaved by ADAMTS13 within the A2 domain at its Tyr[1605]-Met[1606] bond (1, 3, 5, 7, 8). Cleavage is activated by shear when A2 is present in large VWF concatamers, but not when present as the much smaller, isolated domain (5–7). Presumably, this is because the tensile forces acting on proteins in shear flow increase with protein length (9). Shear flow elongates VWF (2), and tensile force exerted on the concatamer is thought to cause conformational changes in A2 domains that enable cleavage (3, 5, 8); the scissile bond is likely buried in the native state (10, 11). Therefore, partial or complete unfolding may be the mechanism for substrate activation (6). Here, by directly applying force with laser tweezers (12, 13) to a single A2 domain, we test the hypothesis that unfolding and folding of the A2 domain may occur at forces that might be experienced by VWF in its transit through the circulation or at sites of hemostasis and thrombosis, and that force acts as a cofactor to unfold A2 for cleavage by ADAMTS13.

Single, N-glycosylated A2 domains coupled to DNA handles through N- and C-terminal Cys tags (fig. S1) were suspended between beads held in a laser trap and micropipette (Fig. 1B). A2 domains were subjected to cycles of force increase, force decrease, and clamping at a low force to enable refolding before the next cycle (Fig. 1C). A2 domain unfolding was marked by abrupt increase in length of the tether between the two beads (Fig. 1C, inset, and 1D, cycle ii). The increase in length at different forces was fitted to the wormlike chain (WLC) model (14) (Fig. 2A), which yielded an A2 contour length of 57 ± 5 nm and a persistence length of 1.1 ± 0.4 nm. A2 N-terminal and C-terminal residues Met[1495] and Ser[1671] are 1 nm apart in the folded state (15). The total length of 58 ± 5 nm divided by an extension length of 0.36 nm per residue yields unfolding of 161 ± 14 residues. This corresponds well to complete unfolding of the predicted 177-residue A2 domain.

Over a range of force loading rates, unfolding force was determined and plotted against the logarithm of the loading rate (Fig. 2B). The fit to a single-barrier kinetic model (16) yields an unfolding rate in the absence of force, k_u^0, of 0.0007 s^{-1} (confidence band of 0.0002 s^{-1} to 0.003 s^{-1}), and a force scale, f_β, which exponentially increases the unfolding rate $k_u = k_u^0 exp(f/f_\beta)$, of 1.1 ± 0.2 pN.

A subset of about 20% of unfolding events included a discernible pause [defined by four or more data points at a short-lived (fig. S3), partially unfolded intermediate state], which was directly observed in force-extension curves (Fig. 2C). Fit to the WLC model of the A2 extension distances (Fig. 2C, inset) shows that the intermediate state usually lies 40% of the distance between the fully folded and unfolded states.

During the pause at a clamped force between each cycle of force decrease and increase, the A2 domain had the opportunity to refold (Fig. 1C). Subsequent unfolding revealed folding during the pause (Fig. 1, C and D, cycle ii), whereas a lack of unfolding suggested an absence of refolding
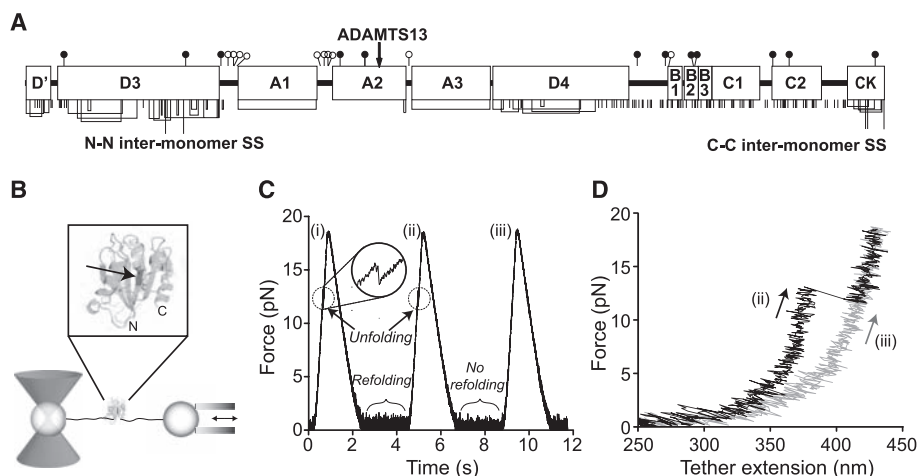

Fig. 1. A2 domain unfolding and refolding with laser tweezers. (**A**) Domain organization of VWF. Cysteines and disulfide bonds are shown beneath, and N- and O-linked sites above as filled and open lollipops, respectively. (**B**) Experimental setup. A2 domain (enlarged in inset with ADAMTS13 cleavage site indicated by an arrow) is coupled to double-stranded DNA handles, which are bound through tags at their other ends to beads held by a laser trap and a translatable (double arrow) micropipette. (**C**) Force on a molecular tether during representative cycles of force increase, decrease, and clamping at a constant low level. (**D**) Force-extension traces during force loading in cycles ii and iii from panel (C).
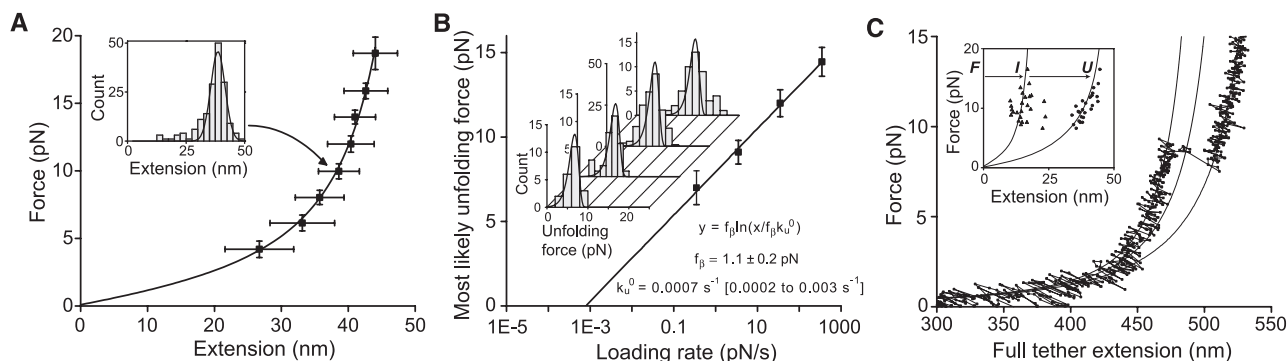

Fig. 2. Unfolding of the A2 domain. (**A**) A2 domain force-extension data with an error-weighted least squares fit to the WLC model (line) (14). Extension distances were sorted by unfolding force into 2-pN bins. A histogram of extensions for each bin (inset) was fitted to a Gaussian curve (inset, solid line) to find peak extension, and force was averaged for that bin. Uncertainty in extension is shown as the half width of the Gaussian fit, and uncertainty in force is shown as 1 SD. (**B**) Unfolding force as a function of loading rate. Unfolding forces were binned by loading rate and plotted as histograms (inset). The peak of each histogram was plotted against the loading rate; uncertainty in y is shown as half of the bin width. A linear fit to the data (line) predicts the distributions of unfolding force (inset, lines), which agree well with the histograms (inset). (**C**) Representative force-extension trace for a tether pausing at an intermediate state, with three WLC curves (solid lines) representing DNA + folded A2, DNA + partially unfolded A2, and DNA + fully unfolded A2. (Inset) Extensions of A2 to intermediate (I) and unfolded (U) lengths fit to the WLC model (lines).

(Fig. 1, C and D, cycle iii). The binary state of the domain was further confirmed with force extension curves, which have distinct branches for the unfolded and folded states (Fig. 1D). The force dependence of refolding (Fig. 3) was fitted by using maximum likelihood to an f^2 model, which takes into account the soft compliance of the unfolded state (16–18): $k_f = k_f^0 exp(-f^2/2\kappa k_B T)$ (where κ is defined as the effective compliance of the unfolded state, k_B is the Boltzmann constant, and T is the absolute temperature) (see also fig. S3). We found a refolding rate in the absence of force, $k_f^0 = 0.54 \pm 0.05$ s^{-1}, and compliance, $\kappa = 0.18 \pm 0.04$ pN/nm.

Using the folding and unfolding rates in the absence of force, we can estimate the free energy difference between the two states: $\Delta G = -k_B T \cdot \ln(k_u^0/k_f^0) = 6.6 \pm 1.5\ k_B T$ (3.9 ± 0.9 kcal/mol). This is close to the ΔG of $5.9 \pm 0.8\ k_B T$ (3.5 ± 0.5 kcal/mol) estimated from urea-induced unfolding of an *Escherichia coli* A2 fragment (19).

To test the hypothesis that A2 unfolding is required for cleavage by ADAMTS13, A2 was mechanically unfolded in the absence or presence of ADAMTS13 and relaxed to a clamped force of 5 pN (Fig. 4A). At this force, the lifetime of the unfolded state is >140 s, which makes refolding unlikely during the incubation with ADAMTS13. Cleavage by ADAMTS13 was detected as a drop in force on the tether to 0 pN (Fig. 4A, left). Spontaneous rupture at 5 pN, i.e., the background with no enzyme (Fig. 4A, right), was rare (Fig. 4B, inset). In experiments with a lower force ramp, unfolding sometimes did not occur, as shown by lack of the characteristic force-extension signature. No cleavage of folded A2 at 5 pN with 100 nM or 1 µM enzyme was observed.

With unfolded A2 in the presence of enzyme, the fraction of surviving tethers decreased exponentially with time, which demonstrated first-order reaction kinetics and yielded the time constant τ for cleavage at three different enzyme concen-

trations (Fig. 4B, inset). The observed enzymatic rate, i.e., reciprocal of τ, was fitted with the single-molecule Michaelis-Menten equation (20), $1/\tau = k_{cat}$[ADAMTS13]/([ADAMTS13] + K_M) (Fig. 4B).

As the largest known soluble protein, VWF has more force exerted on it than any other free protein in the vasculature. Hydrodynamics and the overall shape and orientation of VWF multimers in flow are relevant to understanding the tensile force exerted on A2 domains within ULVWF and trimming by ADAMTS13 (5). In shear flow, the rate of fluid flow increases from the wall toward the center (Fig. 5, A and B). The product of shear rate and viscosity, shear stress (in units of force per area), imparts force to particles in shear flow that is related to their surface area. Compared with VWF free in flow, the hydrodynamic force at a given shear is much higher on VWF immobilized on a vessel wall or bridging two platelets free in flow and, at intermediate levels, for VWF bound to a single platelet free in flow (9, 21). Because of weak attractive interactions between domains within each multimer, VWF multimers have an overall compact, yarn ball–like shape in stasis (2, 22–24). Above a critical shear stress of 50 dyn/cm^2 (13), the attractive forces are overcome by hydrodynamic drag, and VWF free in flow periodically elongates and contracts (2, 24) (Fig. 5C). Shear flow can be conceptualized as the superposition of rotational flow and elongational flow (Fig. 5B). The rotational flow causes particles to tumble (Fig. 5C). Tumbling is more evident for polymers such as DNA (25); the attractive forces between VWF monomers appear to keep it largely zipped up during tumbling, with alternating cycles of elongation and compaction that demonstrate tumbling (Fig. 5C) (2, 24).

We apply concepts from the field of polymer dynamics to VWF. For an extended VWF multimer with N monomers, the tensile force on a monomer increases with distance from the nearest end of the multimer (Fig. 5D), and force at the middle of the multimer is proportional to N^2 (Fig. 5D) [see estimation of force within VWF (13)] (26). Force increases with the square of length because both multimer size and the

difference in velocity between shear lamina, in which the two ends of the multimer find themselves, increase with length (9, 13, 26). This second-power dependence not only has important implications for unfolding of the A2 domain and cleavage by ADAMTS13 (Fig. 5D), but also explains the much greater potency of longer than shorter VWF multimers in shear-induced aggregation of platelets in hemostasis and thrombosis (1, 5).

Could the tensile force on VWF free in the circulation reach levels in vivo sufficient to explain unfolding of the A2 domain and cleavage by ADAMTS13? The tensile force is estimated [see tumbling time scale (13)] to reach 10 pN in the middle of a VWF 200-monomer multimer at the maximal shear stress of 100 dyn/cm^2 (shear rate of 5000 s^{-1}) found in healthy vessels in vivo (5, 27) (Fig. 5D). Using a loading rate of 25 pN/s estimated from the VWF tumbling rate in shear (13), the A2 domain typically unfolds at about 11 pN (peak of the unfolding force distribution) (Fig. 2B). The upper size limit of VWF in the circulation is variously estimated to correspond to a 100-monomer multimer (1) or a 200-monomer multimer (2, 13, 22, 23). Thus, our single-molecule data on the A2 domain successfully predicts the observed upper size limit of VWF multimers in vivo as ~200 monomers (Fig. 5D). Caveats include uncertainty in the angle of maximally extended VWF with respect to flow direction, which could influence the magnitude of the peak force estimate by several fold [see peak force on relaxing, extending VWF (13)], simplifying assumptions made in the calculations, and a possible contribution of platelets to VWF trimming (21, 28). The dynamics of VWF in shear flow is an important area of future investigation for understanding susceptibility to ADAMTS13, as well as activation in hemostasis.

The existence of a clear threshold for the lengths of VWF multimers has been shown in vivo; a bolus of ULVWF released from endothelium into the circulation is trimmed to the preexisting equilibrium length distribution of circulating VWF multimers within 2 hours by ADAMTS13 (4). Our
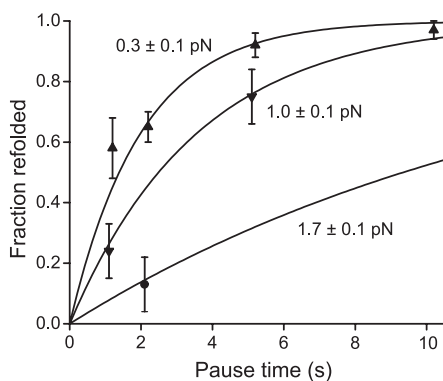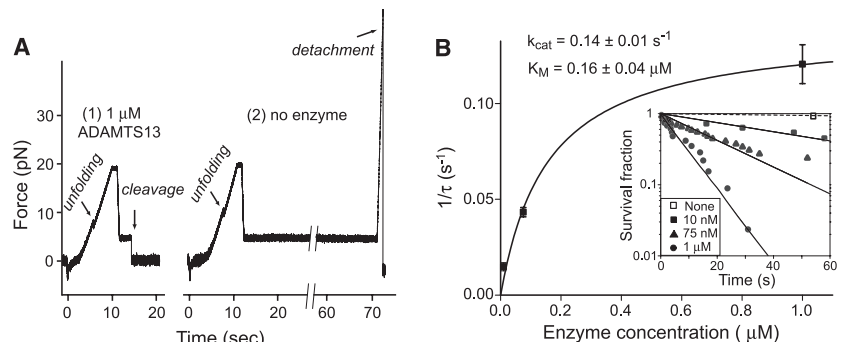

Fig. 3. A2 domain refolding kinetics. Binary refolding events were binned by clamp force and time. Standard errors (bars) were calculated as $(p \cdot (1 - p)/n)^{0.5}$, where p is fraction refolded and n is number of events. Overlaid on the data are the exponential curves predicted by maximum likelihood estimation (i.e., on the data without binning) using the $\tau \approx exp(f^2)$ model.

Fig. 4. Mechanoenzymatic cleavage of A2 by ADAMTS13. (**A**) Representative traces showing cleavage in the presence of enzyme (left) and no cleavage in the absence of enzyme (right). (**B**) Enzyme kinetics. The hyperbolic dependence of catalytic rate on enzyme concentration was fitted with the single-molecule Michaelis-Menten equation (20) (solid line). Data points and standard error were determined from single-parameter exponential fits to the survival fraction as a function of time (inset).
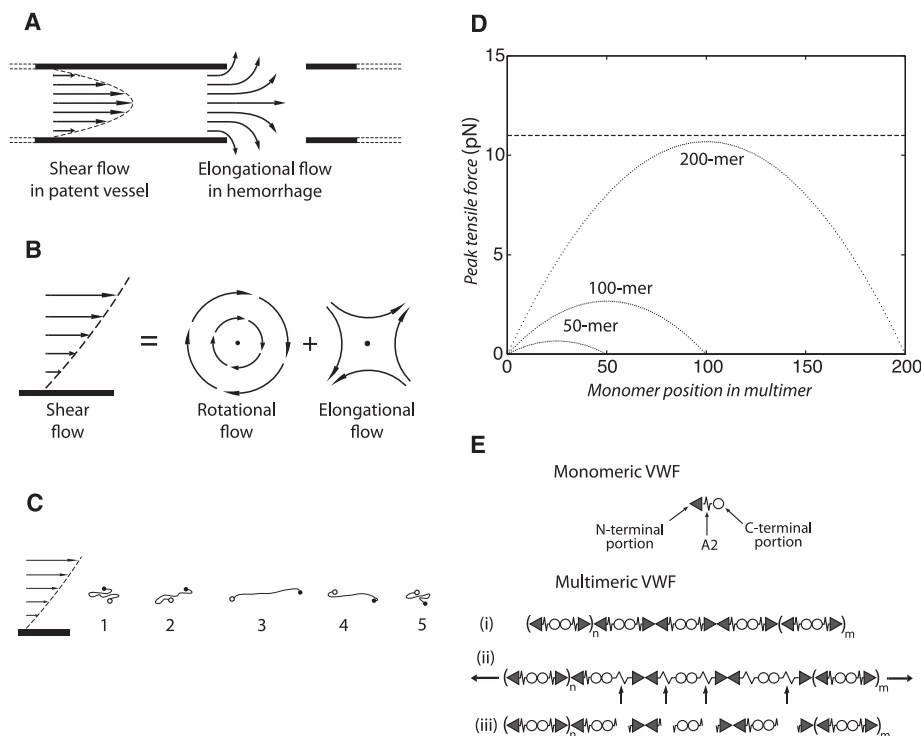
Fig. 5. Model for mechanoenzymatic cleavage of ULVWF in the circulation. (**A**) Shear flow in a vessel and elongational flow at a site of bleeding. (**B**) Shear flow may be represented as elongational flow superimposed on rotational flow [modified from (*25*)]. (**C**) Cartoon of VWF elongating, compressing, and tumbling in shear flow. (**D**) Peak force as function of monomer position in a VWF multimer chain of 200, 100, or 50 monomers at 100 dyn/cm². Dashed line shows the most likely unfolding force for the A2 domain at a loading rate of 25 pN/s. (**E**) Schematic of VWF, with N-terminal end as triangle, A2 as spring, and C-terminal end as circle. Elongation results in unfolding of some A2 domains, some of which are cleaved (arrows). The resulting fragments are shown.

analysis illustrates the principles that dictate the maximum length of circulating VWF multimers in vivo and suggests that the force on VWF free in the circulation is sufficient to induce unfolding of the A2 domain and cleavage by ADAMTS13.

Another concept from polymer dynamics (*25*) important for VWF is elongational flow (Fig. 5, A and B). Close to a site of hemorrhage, flow will transition from shear flow, which has both rotational and elongational components (Fig. 5A, left), to elongational flow (Fig. 5A, right). Although the actual flow pattern would be complex, the overall picture is that tumbling and alternating cycles of compression will tend to cease, and VWF will only experience elongation. Alignment of VWF with the principal direction of elongational strain could increase peak tensile force to about 10 times that experienced in shear flow [see force on VWF in elongational flow (*13*)].

We have definitively established that unfolding is required for cleavage of the A2 domain by ADAMTS13. In a portion of unfolding events, we observed an intriguing transient intermediate state. In VWF A2, the N-terminal β1 strand is central in the fold, whereas the C-terminal α6 helix is peripheral. Therefore, unfolding induced by elongational force will begin at the C terminus (*15*). Unfolding of 40% of the contour length in the intermediate state would thus correspond to the unfolding of about 70 C-terminal residues, up to

and including the β4 strand, which contains the scissile Tyr^{1605}-Met^{1606} peptide bond. Studies with peptide fragments show that C-terminal, but not N-terminal, segments distal from the cleavage site are recognized by ADAMTS13 (*29*). Thus, it is possible that ADAMTS13 could recognize and cleave the intermediate unfolded state.

Our single-molecule k_{cat} for the ADAMTS13 enzyme of 0.14 s^{-1} is in the range of 0.14 to 1.3 s^{-1}, determined in bulk phase with unfolded peptide substrates corresponding to the C-terminal 70 residues of A2 (*11, 30*). However, our K_M of 0.16 μM is lower than previous estimates of 1.7 and 1.6 μM (*11, 30*). The lower K_M value determined here may reflect a more physiologic state of the substrate. Notably, different domains within ADAMTS13 recognize different portions of the unfolded peptide substrate that are far apart in sequence (*29, 30*). Whereas peptide substrates have essentially random configurations, tension applied to the unfolded A2 domain partially orders it in one dimension, and this more linear configuration may improve recognition by the different domains within ADAMTS13.

VWF will only be exposed to peak shear intermittently during each tumbling cycle and only to high shear during transit through arterioles and capillaries. The lifetime of about 2 s of the unfolded state in the absence of force is longer than the time period of peak force exposure (*9, 13*)

and provides a window of opportunity for cleavage by ADAMTS13. Refolding to the correct low-energy state of the A2 domain after tension is released is another property important for function in vivo. Aberrant refolding could permit cleavage by ADAMTS13, as is observed with some A2-domain preparations from *E. coli* (*31*).

Our single-molecule enzyme assays suggest that the rate of VWF cleavage is limited by ADAMTS13 concentration in vivo, which, at 6 nM (*32*), is substantially below the K_M of 160 nM and yields a time scale for cleavage in vivo of ~200 s. Although the numbers may be altered for cleavage of unfolded A2 within intact VWF, these rough estimates are relevant to understanding events in vivo. Thus, over the short time periods of <1 s important in hemostasis, binding of VWF through the A1 domain to GPIb on platelets and through the A3 domain to collagen on the subendothelium should win out over cleavage of the A2 domain by ADAMTS13.

A further wrinkle is added by a *cis*-proline recently discovered in the A2 structure (*15*) consistent with a small number of A2 tethers that suddenly stopped refolding and, after a long delay, resumed refolding (*13*). VWF, bound to platelets at sites of hemorrhage, would be exposed to forces sufficient to accelerate cis-to-trans peptide isomerization (*33*) in unfolded A2. A *trans*-proline would be a long-lasting (100- to 1000-s) impediment to refolding that would enhance cleavage by ADAMTS13 during wound repair.

The A2 domain's unique lack of protection by disulfide bonds within VWF (Fig. 1A) and low resistance to unfolding suggest that A2 has evolved to be the shear bolt domain of VWF. A shear bolt breaks above a designed force threshold, so as to protect other parts of a machine from accidental damage. Similarly, the A2 domain unfolds when present in VWF multimers that experience high-tensile force and is cleaved by ADAMTS13, which results in down-regulation of hemostatic activity.

References and Notes
1. J. E. Sadler, *Annu. Rev. Biochem.* **67**, 395 (1998).
2. S. W. Schneider *et al.*, *Proc. Natl. Acad. Sci. U.S.A.* **104**, 7899 (2007).
3. J. E. Sadler, *Annu. Rev. Med.* **56**, 173 (2005).
4. J. Batlle *et al.*, *Blood* **70**, 173 (1987).
5. H. M. Tsai, *Semin. Thromb. Hemost.* **29**, 479 (2003).
6. H. M. Tsai, *Blood* **87**, 4235 (1996).
7. M. Furlan, R. Robles, B. Lamie, *Blood* **87**, 4223 (1996).
8. J. F. Dong *et al.*, *Blood* **100**, 4033 (2002).
9. H. Shankaran, S. Neelamegham, *Biophys. J.* **86**, 576 (2004).
10. J. J. Sutherland, L. A. O'Brien, D. Lillicrap, D. F. Weaver, *J. Mol. Model.* **10**, 259 (2004).
11. S. Zanardelli *et al.*, *J. Biol. Chem.* **281**, 1555 (2006).
12. J. R. Moffitt, Y. R. Chemla, S. B. Smith, C. Bustamante, *Annu. Rev. Biochem.* **77**, 205 (2008).
13. Materials and methods are available as supporting material on *Science* Online.
14. C. Bustamante, J. F. Marko, E. D. Siggia, S. Smith, *Science* **265**, 1599 (1994).
15. Q. Zhang, Y.-F. Zhou, C.-Z. Zhang, T. A. Springer, *Proc. Natl. Acad. Sci. U.S.A.*, 10.1073_pnas.0903679106 (2009).
16. E. Evans, K. Ritchie, *Biophys. J.* **72**, 1541 (1997).

17. P. Hanggi, P. Talkner, M. Borkovec, *Rev. Mod. Phys.* **62**, 251 (1990).
18. E. Evans, K. Halvorsen, K. Kinoshita, W. P. Wong, in *Handbook of Single-Molecule Biophysics*, P. Hinterdorfer and A. van Oijen, Eds. (Springer, New York, in press).
19. M. Auton, M. A. Cruz, J. Moake, *J. Mol. Biol.* **366**, 986 (2007).
20. S. C. Kou, B. J. Cherayil, W. Min, B. P. English, X. S. Xie, *J. Phys. Chem. B* **109**, 19068 (2005).
21. K. Shim, P. J. Anderson, E. A. Tuley, E. Wiswall, J. E. Sadler, *Blood* **111**, 651 (2008).
22. W. E. Fowler, L. J. Fretto, K. K. Hamilton, H. P. Erickson, P. A. McKee, *J. Clin. Invest.* **76**, 1491 (1985).
23. H. Slayter, J. Loscalzo, P. Bockenstedt, R. I. Handin, *J. Biol. Chem.* **260**, 8559 (1985).
24. A. Alexander-Katz, M. F. Schneider, S. W. Schneider, A. Wixforth, R. R. Netz, *Phys. Rev. Lett.* **97**, 138101 (2006).
25. D. E. Smith, H. P. Babcock, S. Chu, *Science* **283**, 1724 (1999).
26. J. A. Odell, A. Keller, *J. Chem. Phys.* **88**, 4022 (1988).
27. Z. M. Ruggeri, G. L. Mendolicchio, *Circ. Res.* **100**, 1673 (2007).
28. P. J. J. van Genderen, U. Budde, J. J. Michiels, R. van Strick, H. H. D. M. van Vliet, *Br. J. Haematol.* **93**, 962 (1996).
29. W. Gao, P. J. Anderson, J. E. Sadler, *Blood* **112**, 1713 (2008).
30. W. Gao, P. J. Anderson, E. M. Majerus, E. A. Tuley, J. E. Sadler, *Proc. Natl. Acad. Sci. U.S.A.* **103**, 19099 (2006).
31. J. L. Whitelock *et al.*, *J. Thromb. Haemost.* **2**, 485 (2004).
32. H. B. Feys *et al.*, *J. Thromb. Haemost.* **4**, 955 (2006).
33. A. Valiaev, D. W. Lim, T. G. Oas, A. Chilkoti, S. Zauscher, *J. Am. Chem. Soc.* **129**, 6491 (2007).

Halofuginone Inhibits T$_H$17 Cell Differentiation by Activating the Amino Acid Starvation Response

Mark S. Sundrud,[1] Sergei B. Koralov,[1] Markus Feuerer,[2] Dinis Pedro Calado,[1] Aimee ElHed Kozhaya,[3] Ava Rhule-Smith,[4] Rachel E. Lefebvre,[1] Derya Unutmaz,[3] Ralph Mazitschek,[5,6,7] Hanspeter Waldner,[4] Malcolm Whitman,[8]* Tracy Keller,[8]* Anjana Rao[1]*

A central challenge for improving autoimmune therapy is preventing inflammatory pathology without inducing generalized immunosuppression. T helper 17 (T$_H$17) cells, characterized by their production of interleukin-17, have emerged as important and broad mediators of autoimmunity. Here we show that the small molecule halofuginone (HF) selectively inhibits mouse and human T$_H$17 differentiation by activating a cytoprotective signaling pathway, the amino acid starvation response (AAR). Inhibition of T$_H$17 differentiation by HF is rescued by the addition of excess amino acids and is mimicked by AAR activation after selective amino acid depletion. HF also induces the AAR in vivo and protects mice from T$_H$17-associated experimental autoimmune encephalomyelitis. These results indicate that the AAR pathway is a potent and selective regulator of inflammatory T cell differentiation in vivo.

Naïve CD4$^+$ T cells differentiate into diverse effector and regulatory subsets to coordinate immunity to pathogens while establishing peripheral tolerance. Besides T$_H$1 and T$_H$2 effector subsets, which produce interferon-γ (IFN-γ) and interleukin-4 (IL-4), respectively, naïve T cells can differentiate into proinflammatory T helper 17 (T$_H$17) cells or tissue-protective induced T regulatory (iT$_{reg}$) cells (1, 2). T$_H$17 cells are key regulators of autoimmune inflammation; charac-

teristically produce IL-17 (IL-17A), IL-17F, and IL-22; and differentiate in the presence of inflammatory cytokines, such as IL-6 or IL-21, together with transforming growth factor–β (TGF-β) (1, 2).

The small molecule halofuginone (HF) is a derivative of the plant alkaloid febrifugine (3). HF has shown therapeutic promise in animal models of fibrotic disease and a clinical trial for scleroderma (3–5), but its mechanism of action is unclear. To investigate whether HF could modulate T cell differentiation, we stimulated murine T cells to induce T$_H$1, T$_H$2, iT$_{reg}$, or T$_H$17 differentiation and treated these cells with HF or an inactive derivative, MAZ1310 (fig. S1, A and B) (6). HF selectively inhibited the development of T$_H$17 cells with a median inhibitory concentration (IC$_{50}$) of 3.6 ± 0.4 nM (Fig. 1A and fig. S2A). Low concentrations of HF that impaired T$_H$17 differentiation did not influence T$_H$1, T$_H$2, or iT$_{reg}$ differentiation (Fig. 1A and fig. S2A) and had no impact on T cell receptor (TCR)–induced cytokine secretion by naïve T cells (fig. S2B). HF also repressed IL-17 expression by human T cells without influencing IFN-γ production (Fig. 1B). Consistent with a previous report (7), 10-fold higher

concentrations of HF broadly impaired lymphocyte function (Fig. 1A and fig. S2C). Inhibition of T$_H$17 differentiation by HF was most pronounced when added within the first 24 hours of culture (Fig. 1C), was stereospecific (fig. S2D), and was not cytotoxic below 100 nM (fig. S2E). Although HF treatment delayed S-phase entry within 24 hours of TCR activation, these T cells recovered thereafter, showing no defect in expansion kinetics between days 2 and 4 postactivation (fig. S3). Moreover, HF suppressed T$_H$17 differentiation, irrespective of the number of cell divisions completed (Fig. 1D), and reduced T$_H$17 differentiation when IFN-γ and IL-4, cytokines that inhibit T$_H$17 differentiation (8), were neutralized by antibodies (fig. S4A).

HF inhibited *Il17a* and *Il17f* mRNA production without affecting the expression of IL-2 and tumor necrosis factor, cytokines expressed by all effector T cells (fig. S4B). HF treatment did not affect the induction of RORγt and RORα, two orphan nuclear receptors induced by T$_H$17 polarizing cytokines that mediate lineage commitment (9, 10) (fig. S4C). Ectopic expression of RORγt in T cells did not override the inhibitory effects of HF on T$_H$17 differentiation (fig. S4D), confirming that RORγt is not sufficient to drive the effector function of T$_H$17 cells (11).

HF did not directly inhibit signaling induced by TGF-β or IL-6, the two principal cytokines that instruct T$_H$17 differentiation. Although high concentrations (>50 nM) of HF were reported to impair TGF-β signaling in fibroblasts (4), low doses of HF that repress T$_H$17 differentiation inhibited neither TGF-β–induced R-Smad2 phosphorylation (fig. S5A) nor a variety of other lymphocyte responses to TGF-β (fig. S5, B to D) (12). In contrast, the type 1 TGF-β receptor kinase inhibitor SB-431542 (fig. S1C) abrogated all responses to TGF-β (fig. S5). Additionally, HF did not inhibit early IL-6–induced STAT3 phosphorylation (where STAT proteins are signal transducers and activators of transcription) (fig. S6), but it did reduce sustained STAT3 activation beginning 12 hours poststimulation (fig. S6), indicating that HF indirectly modulates factors that maintain STAT3 signaling. Consistent with decreased STAT3 activity (13), HF-treated T$_H$17 cells

[1]Department of Pathology, Harvard Medical School and Immune Disease Institute, Boston, MA 02115, USA. [2]Section on Immunology and Immunogenetics, Joslin Diabetes Center, Boston, MA 02215, USA. [3]Department of Microbiology and The Microbial Pathogenesis Program, New York University School of Medicine, New York, NY 10016, USA. [4]Department of Microbiology and Immunology, Pennsylvania State University College of Medicine, Hershey, PA 17033, USA. [5]Chemical Biology Program, Broad Institute, Cambridge, MA 02142, USA. [6]Department of Biological Chemistry and Molecular Pharmacology, Harvard Medical School, Boston, MA 02142, USA. [7]Chemical Biology Program, Broad Institute, Cambridge, MA 02142, USA. [8]Department of Developmental Biology, Harvard School of Dental Medicine, Boston, MA 02115, USA.

*To whom correspondence should be addressed. E-mail: whitman@hms.harvard.edu (M.W.); tkeller@hms.harvard.edu (T.K.); arao@idi.harvard.edu (A.R.)

Supporting Online Material for

Mechanoenzymatic Cleavage of the Ultralarge Vascular Protein von Willebrand Factor

Xiaohui Zhang, Kenneth Halvorsen, Cheng-Zhong Zhang, Wesley P. Wong,
Timothy A. Springer*

*To whom correspondence should be addressed. E-mail: springer@idi.harvard.edu
(T.A.S.) or wong@rowland.harvard.edu (W.P.W.)

This PDF file includes

Supporting Online Materials

Materials and Methods

Protein expression. The cDNA of human VWF A2 domain (Pro[1480] to Pro[1678] with pre-pro-VWF numbering) was PCR-amplified with or without additional cysteines flanking the N and C termini added using PCR primers (Fig. S1a). All cDNAs were cloned into the Age I and Xho I sites of plasmid pHLsec (*1*), which encodes an N-terminal secretion signal sequence and a C-terminal His$_6$ tag. Plasmids were transfected to HEK293T cells using lipofectamine reagent (Invitrogen). Culture supernatants were harvested after 5 days of transfection and proteins were purified using Ni-NTA affinity chromatography followed by size-exclusion chromatography in 155 mM NaCl, 3 mM Na$_2$HPO$_4$, 1 mM KH$_2$PO$_4$ (PBS).

Sample preparation. Two 802-bp DNA handles were generated by PCR with Vent DNA polymerase (New England Biolabs) in 20 mM DTT with pGEMEX 1 plasmid DNA as template (Promega) and the primer 5'thiolmodifier C6-SS- CGA-CGA-TAA-ACG-TAA-GGA-CAT-C and either 5'biotin- or 5'digoxigenin-CAA-AAA-ACC-CCT-CAA-GAC-CC primers (1 µM). Handles were activated and coupled to protein through disulfide bonds by modification of a previously published procedure (*2*). PCR products (10 ml) were purified using HiSpeed Plasmid Maxi Kit (Qiagen) according to the manufacturer's protocol with the following modifications. PCR reaction product was diluted 10-fold with QBT buffer (Qiagen) and applied to pre-equilibrated Qiagen HiSpeed Maxi Tips. Tips were washed with 60 ml of Buffer QC to remove DTT. DNA was eluted with 15 ml of Buffer QF and immediately mixed with 0.3 ml 50 mM 2,2'-dithio-dipyridine (DTDP) in DMSO to activate the 5'thiol. Kinetics of release of pyridine-2-thione following activation by DTDP was monitored by absorbance at 343 nm. Derivatized DNA was purified away from excess DTDP by precipitation with 10.5 ml isopropanol, followed by passing through QIAprecipitator module, and three washes with 2 ml 70% ethanol. Derivatized DNA was eluted with 1 mM EDTA in water (pH 8), concentrated 10-fold, and stored at -80°.

Typically, 30 µM of cysteine-modified A2 protein (50 µL) was treated with 1 mM DTT for 1 hour under argon at room temp. DTT was removed by passing the A2 protein twice through 0.5 ml Zeba desalting columns (Pierce) in argon. About 5 µM of A2 domain was allowed to react with 10 µM DTDP-activated DNA handles in 0.2M sodium acetate, pH 5, under argon for 16 hours. Coupled material (typically 75 µL) was neutralized by adding 8.3 µL 1 M Tris pH 8.5, and stored at -80°.

Carboxyl-polystyrene 2.8 µm beads (10 mg, Spherotech, Lake Forest, IL) were washed and resuspended in 0.2 mL 50 mM 2-[N-morpholino]ethanesulfonic acid pH 5.2, 0.05% ProClin 300 (Bangs Labs, Fishers, IN). 1-ethyl-3-(3-dimethylaminopropyl)carbodiimide (2 mg in 10 µL of the same buffer) was added, followed after 5 min by 50 µg of 5 mg/ml streptavidin or 1mg/ml affinity-purified sheep anti-digoxigenin IgG (Roche) in PBS. After shaking for 1 hour at room temperature, beads were washed 5 times in PBS and stored at 4° C in PBS supplemented with

0.02% Tween 20 and 2 mM sodium azide.

Instrument description. The force probe used in this experiment is based on an optical trap and a piezo-controlled micropipette (Fig. 1a), functionally identical to a previously described instrument (*3*). The 1-D position of beads held by the trap and the pipette are determined with an accuracy of +/- 2nm at 1,000 fps. The optical trap was calibrated using the blur-corrected power spectrum fit (*4*). Spring constants ranged from 0.04-0.1pN/nm.

Single molecule experiments. Experiments were performed at room temperature in TBS (20 mM Tris, 150 mM NaCl, pH 7.5). A force calibration was performed for each bead; both the calibration and experiments were performed at 20 μm from the cover glass. Custom software (Labview) controlled piezo motion and data acquisition. Experiments were performed by bringing the test bead into feedback-controlled contact with the probe bead (typically 3 pN for 0.1 seconds) and subsequently retracting the test bead at a constant speed. Upon formation of a molecular tether, the tether was repeatedly stretched and relaxed between two forces with varying pauses at the low force to observe refolding. Retraction was performed at 4 different rates corresponding to roughly 0.35, 3.5, 35, and 350 pN/s.

Data analysis. The presence of a single molecular tether between the two beads was verified by comparing the distance between the two beads (i.e., tether extension) with the expected distance of two 802 bp DNA linkers in series (i.e., ~500 nm). Tethers with half or less of the expected length were discarded. Tethers were further filtered based on each tether's consistency with overall worm like chain behavior. Specifically, all events were discarded from tethers that had more than 5% of unfolding events falling outside +/- 7 nm band of the worm-like chain model (~2 standard deviations from the mean, Fig. 2a). Approximately 55% of all tethers met these strict criteria.

Material properties of unfolded A2 were determined from the multi-part force-extension curves of the molecule construct, as illustrated in Figure 2. For example, to measure the contour length of the intermediate state, the left-most part of the curve was fit with a single worm-like chain, representing DNA plus folded A2, as in Figure 2c. The second and third parts were fit with another worm-like chain in series with the first, modeling partially or fully unfolded A2, respectively, with the WLC parameters for unfolded A2 determined from the results of figure 2a.

After repeated cycles of force increase and decrease, constructs would often pause for long periods of time in the unfolded state (after putative cis-trans isomerization, see below). To avoid biasing the refolding statistics in these cases, refolding events were counted up to but not including the last positive refolding statistic.

Enzyme cleavage assay. Recombinant human ADAMTS13 (R&D Systems) was added at the indicated concentration in TBS buffer supplemented with 20 μM Zn^{2+}, 100 μM Ca^{2+} and 0.1% BSA. Single A2 molecules were stretched to 20 pN, then relaxed to a constant force of 5 pN for 60 sec; alternatively, for the folded A2 domain, the stretch to 20 pN followed the constant force. If no cleavage was found after 60 s incubation, the assay was terminated by ramping up

force until the tether was broken, presumably by rupture of the digoxigenin-Fab or biotin-streptavidin linkages between the tether and beads (Fig. 4a, panel 2).

SOM Text

Cis-trans and trans-cis peptide isomerization. During the refolding experiments, tethers sometimes failed to refold for many cycles of the force protocol shown in Fig. 1c. In rare cases those tethers subsequently resumed refolding after a long delay. After data collection for this project was completed, an A2 crystal structure revealed a cis-Pro residue (*5*). Since cis-peptide isomerization is generally rate-limiting for protein folding, with a typical lifetime of 100 s in the absence of prolyl isomerases (*6*), we examined the kinetics of these events for consistency with cis-Pro isomerization. To estimate the kinetic rates between the putative cis and trans states, we fit the respective time distributions with single exponential decays using a maximum likelihood estimator with censoring.

For the forward rate from cis to trans, the observed and censored times were measured from tether formation to cessation of refolding and end of experiment, respectively. This yields a forward conversion time of 96 seconds, with a 1 SD confidence band of 77 to 126 seconds. For the reverse rate from trans to cis, the observed and censored times were measured from the last refolding event before cessation to the first new refolding event and end of experiment, respectively. This yields a reverse conversion time of 530 seconds with a confidence interval of 320 to 1490 seconds.

Our analysis assumes that the forces we applied had a negligible effect on the cis-trans conversion kinetics, as the expected force scale is much greater than the ~15 pN maximum force that we used during these experiments [e.g., for a length scale of 1 angstrom, the force scale for the cis-trans transition would be ~$k_BT/0.1$ nm = 40 pN; additionally, AFM experiments observed the transition in the much larger force range of ~ 200-260 pN (*7*)]. Also, the measured time intervals used in the maximum likelihood analysis include both the folded and unfolded configurations since the moment of refolding is not observed directly. While this may result in an overestimate of the conversion times if the isomerization can only occur in the unfolded state, this estimate is not too far off since the force protocols we used caused the tether to spend most of its time in the unfolded state. Despite these simplifications, our simple analysis shows kinetics consistent with those previously reported in other unfolded proteins for cis-trans isomerization (*6*).

Estimation of force within VWF.

Length estimate. Based on the contour length of 60 nm seen for a VWF monomer in EM (*8, 9*), a string extended in shear flow to 15 μm (*10*) would be estimated to contain about 250 monomers. A commonly cited size estimate of 20,000,000 M_r corresponds to about 100 monomers (*11*). We use estimates of 200 monomers in this section to provide an example of

calculations.

Force on a rigid, extended VWF multimer. We first extended the model of Shankaran *et al.* (*12*) from a VWF dimer to VWF multimers. Shankaran *et al.* model a VWF dimer as a dumbbell with two spheres of radius a = 13 nm separated by a rigid tether of length *d* = 94 nm. This is based on the contour length of a VWF dimer in EM of 120 nm (*d* + 2*a*), and its content of globular A and D domains separated by a tether of B and C domains (*11*). The force on any dimer within the multimer was calculated as the sum of the hydrodynamic forces on all dumbbells that were more outward (toward the ends); the forces on the more inner dumbbells do not apply to more outward dumbbells because of force balance. Thus, for calculation, the spheres in the chain are paired off from the ends of the chain, e.g., for a 10 element chain with 5 dimers: 5-4-3-2-1-1-2-3-4-5. The tensile force *F*(*j*) to the inside of any sphere pair *j* in a chain with *N* dimers or pairs, is the sum of the force on all the outer dimer pairs, i.e., total tensile force is

$$F(j) \approx \sum_{i=j}^{N} f(i \times (d + 2a))$$

where *f*(*x*) is the normal force between two spheres that are a distance *x* apart and is given by (*12*) as F_n. Shankaran *et al.* plot the dimensionless F_n proportionality factor, α_n, versus the dimensionless separation, $\delta = d/a$, in their Fig. 3A. Since α_n is proportional to δ in the range $\delta \gg 1$ relevant for VWF, the tensile force formula can be simplified to

$$F(j) \approx \frac{(N+j)(N+1-j)}{2} f(d + 2a)$$

and *f*(*x*) evaluated according to Fig. 3A of Shankaran *et al.* (*12*).

Note from this formula that the normal force on a monomer in the center of a multimer is approximately proportional to N^2 (i.e., when *j*=1), whereas the force on a monomer at the end of a multimer is proportional to *N* (i.e., when *j* = *N*). Although these conclusions had not previously been stated in the VWF literature, a search of polymer physics literature revealed articles describing calculations of the force on monomers within a polymer in flow, e.g. (*13, 14*), where these conclusions had been found.

Using the equation in Shankaran *et al.* for the maximal normal force $F_n = \alpha_n \mu \gamma a^2$, where μ is fluid viscosity, γ is shear rate and *a* is the 13 nm radius of the VWF monomer sphere described above, we determined the force on the A2 domain within any monomer in the multimer. For example, the maximal normal force on the dimer at the center of a maximally extended VWF 200-mer at a 45° angle with respect to flow direction at a shear stress of 100 dyn/cm^2 is estimated to be 220 pN.

While Shankaran *et al.* assumed the VWF glycoprotein monomer can be treated as a 26-nm diameter sphere, there are more accurate ways to estimate the appropriate hydrodynamic sphere size. Assuming a typical, protein-like partial specific volume of 0.7 for the 240,000 M_r VWF glycoprotein monomer yields a volume of 280 nm^3. Assuming that this volume is

contained within 6 equal spheres, corresponding to the number of globular A and D domains in VWF, gives 6 spheres with a total surface area of 370 nm^2. Since hydrodynamic force is related to surface area, another calculation was done with a single sphere that would have the same surface area of 370 nm^2, i.e., with $a = 5$ nm and $d = 110$ nm. This yielded another estimate of the force of 100 pN on a maximally extended 200-mer at a 45° angle with respect to flow direction at 100 dyn/cm^2, which is lower but the same order of magnitude as the above estimate of 220 pN. It is important to note that these calculations reflect the maximum tension at the center of a rigid multimer. A more realistic model of flexible VWF multimers yields a significantly lower tension, as discussed in a later section.

To obtain an alternative estimate of the tension in rigid multimeric VWF, we have performed a similar calculation with a slightly different model. A hydrodynamic shear can be decomposed into a rotational and an elongational part with equal amplitudes, which results in a periodic tumbling motion (*15*). The stretching force on the polymer is primarily due to the elongational part and here we have re-derived the elongational force on the VWF multimer following (*13*). The VWF multimer has a "pearl necklace" form: under the elongational force the A and D domains of VWF are globular ("pearls") each with a diameter of about 5 nm, while the other B and C domains are more elongated; the whole dimer is approximately linear with an overall length of 120 nm (*8, 9*). In our calculation, we assume that each dimer is aligned parallel to the elongational direction. At each N-terminal dimer interface, the two sets of five A and D domains are adjacent. Therefore, within a repeating unit, there are 10 connected globular domains that are approximated as a cylinder 50 nm long and 5 nm in diameter. The surface area of 825 nm^2 per dimer cylinder is in a similar range to that estimated above (2×370 nm^2). In our model, each cylinder is connected to the adjacent cylinder by a string of 70 nm; the cylinder plus string forms a basic repeating unit with the appropriate length of 120 nm.

We write the force balance equation between neighboring repeating units as

$$\mathbf{f}^{i+1} + \mathbf{f}^i + \mathbf{f}_H^i = 0$$

where $\mathbf{f}^{i+1}$ and $\mathbf{f}^i$ are the forces due to tension on the *i*-th and (*i*+1)th strings, and $\mathbf{f}_H^i$ is the

hydrodynamic drag force on the *i*-th cylinder. In the Stokes limit each cylinder is being transported by the local velocity $\mathbf{v}^i$, and the hydrodynamic drag on each cylinder of diameter D and length L is given by (*16*)

$$\mathbf{f}_H^i = \zeta \mathbf{v}^i = \frac{2\pi \mu L}{\ln L/D} \mathbf{v}^i$$

where μ is the viscosity of the fluid. In the latter equation, we have assumed that the cylinders are non-interacting in their hydrodynamics. This free-draining approximation is justified, since at the fully extended limit that we are considering, the effect of hydrodynamic coupling between monomers in a linear polymer is negligible (*17*).

In an elongational flow

$$v_z = \dot{\epsilon}z$$

where $\dot{\epsilon}$ is the elongational strain rate, and z is the coordinate. As we are considering the case when the polymer is aligned with the elongational direction (z), and both **f** and **v** are approximately in the same direction, we can express force balance as a scalar equation. With the velocity defined relative to the center of mass of the polymer, which we set to z = 0, we have

$$f^{i+1} - f^i = -\zeta\dot{\epsilon}z = -2H\mu\dot{\epsilon}z(L+T)$$

where f^i is the tension in the i-th string, L is the length of the cylinder, T is the length of the string tether, $L+T$ is the length of the repeating unit, and H is the constant

$$H = \frac{\pi}{\ln L/D}\frac{L}{L+T}$$

We can integrate this equation in the continuum limit, and together with the boundary condition that f vanishes at both ends, we have

$$f(z) = H\mu\dot{\epsilon}\left[\frac{N^2(L+T)^2}{4} - z^2\right]$$

where N is the number of repeating units or number of dimers, z is the distance from the center of the multimer, and $\dot{\epsilon}$ is the elongational stress rate that we can take to be 1/2 of the shear rate γ (*17*). One can easily verify that $f(z)$ vanishes at both ends of the polymer and attains a maximum at the center, $z = 0$.

For a VWF multimer, $L = 50$ nm, $L/D = 10$, and $T = 70$ nm; therefore, $H = 0.569$. For a shear stress of 100 dyn/cm^2, the maximal force (in unit of pN) is 0.71×[total length in unit of microns]^2 (note that the elongational shear rate is half the shear rate). Thus, for a VWF multimer with 100 dimers (120 nm for each dimer), the force is 102 pN. This is almost identical to the previous estimate of 100 pN for a 200-mer with $a = 5$ nm and $d = 110$ nm by our extrapolation of the Shankaran method from a dimer to multimers.

Tumbling time scale. We used several methods to estimate the time scale for tumbling of VWF in shear flow. Using the numerical results of (*12*) in Fig. 5a and extrapolating δ to 2400 for a 200-mer, we get a dimensionless time-period $\tau\gamma/2\pi$ of 1680 (τ and γ are the time period and shearing rate, respectively). The simulation of elongation of a VWF-like polymer in shear flow at a shear 5-fold greater than the threshold for the globule stretch transition in Fig. 2 of (*18*) shows an average dimensionless time-period of 45 for a polymer with an L/D of 50, which translates to a time-period of 2160 for our L/D of 2400 (note that this L/D is for the full 200-mer rather than for the cylinder in single repeating unit as in the section above). Finally, by assuming the VWF to be a rigid ellipsoid with an L/D of 2400, the dimensionless time period would be 2400 (*19*)]. The dimensional time period τ is then obtained as the dimensionless time period divided by γ/2π. For the maximal shear stress in vivo of 100 dyn/cm^2 (*20, 21*) we have an approximate shear rate of 5,000 s^{-1} and a time period close to 2 s for all three estimates above. It should be noted that the tumbling time scale may be much longer than the relevant time scale for

force loading as in Fig. 2D of (*12*), and Fig. 2 of (*18*) . From these figures, we estimate the force loading time to be roughly 20% of the overall tumbling time, or 0.4 seconds.

Shear threshold. There is a weak dependence on length for the shear threshold of the change in VWF shape from yarn ball-like to extended. Studies on whole VWF showed a threshold of 50 dyn/cm^2 for extension to a length of 15 μm (*10*), and no length-dependence for this threshold was described experimentally. However, theory shows that the threshold scales in proportion to the cube root of length (*18*). Thus, for a VWF length 8 times as long, or 120 μm, the threshold would be twice as high, 100 dyn/cm^2. This is in the physiologic range of shear stresses found in vivo. However, arterioles are in the range of 20 to 30 μm in diameter, and thus, other factors would also contribute to the threshold at longer VWF lengths. It is notable that because of the attractive interactions within a VWF multimer, VWF molecules largely remain "zipped up" with their long axes aligned with the flow direction during tumbling, and in movies of single VWF molecules in flow, tumbling is only evident from alternating cycles of extension and compaction of multimers (see supplemental information movie 1 in (*10*)).

Peak force on relaxing, extending VWF. The above force calculations are for a rigid, maximally extended VWF, at the point in tumbling where maximal force would be applied, where the angle is 45° with respect to the direction of flow. This assumes VWF is rigid and remains completely extended during tumbling, as in the Shankaran model where it is a rigid dumbbell (*12*). However, measurements and simulations on VWF show that it extends and relaxes as it alternately experiences elongation and compression during tumbling in shear flow (*10, 18*). During much of the elongation period, VWF has not yet reached its full extension. Simulations (*18*) suggest that maximal extension is not reached until VWF is about 3° from the direction of flow (angle θ). The force at this angle is $\sin(2\theta)$ times the maximal force at 45°, or about 10 % as much. In all of the estimates described above, the estimate of θ is the one for which we have the least precise information. Multiplying the force estimated above of 100 pN by $\sin(2\theta)$ yields a final estimate of the peak force at the middle of a relaxing-extending VWF 200-mer in shear flow at 100 dyn/cm^2 of 10 pN.

Force loading rate for VWF. The estimates above of the forces and time scales for a VWF multimer in flow can be combined to estimate the rate of tension increase within VWF, giving the force-loading rate of the A2 domain in vivo. A simple estimate is obtained by dividing the peak force by the time period of force loading. For example, for a VWF multimer consisting of 200 monomers (i.e., 100 dimers), the loading rate is approximately 25 pN/s. The loading rate depends upon *N,* the number of monomers. As the peak force scales approximately as N^2 and the tumbling time scales approximately with *N*, the loading rate scales approximately with *N*. Thus, the loading rate of a VWF multimer consisting of *N* monomers is approximately *N*/2 pN/s. As an aside, we note that since the most-likely unfolding force of A2 depends approximately logarithmically on the loading rate, change in *N* will only moderately affect most-likely unfolding force.

Force on VWF in elongational flow. When a blood vessel suddenly breaks, blood flow is elongational, and we can assume the velocity profile to be isotropic at this sudden expansion: the velocity near the center of the vessel will remain in the same direction but decreases in magnitude, while that near the severed ends of the vessel will be perpendicular after exit. We can verify that in this regime strain rate is larger than vorticity (rotational rate), therefore according to (*17*), the polymer will be stretched along the direction of the expansion with maximal elongation, and cease to rotate. A simple scaling estimate gives a strain rate of v/D, which is comparable to the strain rate in shear flow. (A detailed analysis, which needs specific treatment of boundary conditions, is beyond the scope of this manuscript.) Therefore, near the severed ends of the blood vessel, the elongation force would be close to the maximum as estimated above, which is about 100 pN at a comparable shear rate of 5000 s^{-1} and shear stress of 100 dyn/cm^2.

Supplemental Figure Legends

Figure S1. VWF A2 domain construct **and coupling to DNA handles.** (**a**). A2 constructs with Pro^{1480} to Pro^{1678} of human VWF with the indicated sequences were made with or without flanking Cys residues at the N- and C-termini and a His$_6$ tag. (**b**) SDS-PAGE of constructs expressed in HEK293T cells. They migrate as broad bands at 30,000 M_r, consistent with utilization of N-linked sites at both Asn^{1515} and Asn^{1574} and processing to complex carbohydrates. (**c**) 4-20% polyacrylamide Tris-borate EDTA gel of constructs coupled to DNA handles. DNA was visualized by staining with SYBR Green I Nucleic Acid Gel Stain (Roche Applied Science). Arrows mark position of DNA handle monomer and dimer, the desired handle-A2-handle product. Coupling through disulfide bonds was demonstrated by reduction with 5% 2-mercaptoethanol, after which only handle monomer was present.

Figure S2. Intermediate state dwell times were binned and fit with exponential decay (solid line) to determine a lifetime of 1.2 +/- 0.2 ms. Error bars represent statistical error [i.e., 1/sqrt(N)]. Only pauses longer than 3.5 ms were analyzed to ensure reliable data.

Fig. S3. Comparison of the (f) and (f^2) models for maximum likelihood estimation of A2 refolding. (**a**) Maximum likelihood estimation was used to fit all of the data (prior to binning) to a simple Arrhenius tau ~ exp(f) model (solid lines), where $k_f = k_f^0 \exp(-f/f_\beta)$; and a tau ~ exp($f^2$) model, where $k_f = k_f^0 \exp(-f^2/2\kappa k_B T)$ (dashed lines), which takes the soft compliance of the unfolded state into account. κ is defined as the compliance of the unfolded state (i.e., the effective spring constant or curvature of the energy landscape). The data binned by force and time is shown for comparison. The f model found $k_f^0 = 0.7$ +/- 0.1 sec^{-1} and $f_\beta = 1.0$ +/- 0.2 pN; the f^2 model found $k_f^0 = 0.54$ +/- 0.05 sec^{-1} and $\kappa = 0.18$ +/- 0.04 pN/nm. It is clear that the two models match well at low force, but deviate significantly even at 1.7 pN. The refolding data at 1.7 pN implies that the f^2 model is more likely, but properly distinguishing the models is outside of the scope of this paper. (**b**) Predicted unfolded fraction of A2 at equilibrium as a function of

force, using for the refolding rate either the f (solid line) or f^2 (dashed line) model. By assuming equilibrium, the unfolded fraction $= k_u/k_f/(1+ k_u/k_f)$.

Supplementary References

1.   A. R. Aricescu, W. Lu, E. Y. Jones, *Acta. Crystallogr. D. Biol. Crystallogr.* **62**, 1243 (2006).

2.   C. Cecconi, E. A. Shank, C. Bustamante, S. Marqusee, *Science* **309**, 2057 (2005).

3.   K. Halvorsen, Boston Univeristy (2007).

4.   W. P. Wong, K. Halvorsen, *Opt. Express.* **14**, 12517 (2006).

5.   Q. Zhang, Y.-F. Zhou, C.-z. Zhang, T. A. Springer, *Proc. Natl. Acad. Sci. U. S .A.* **in press**, (2009).

6.   F. X. Schmid, *Annu. Rev. Biophys. Biomol.* **22**, 123 (1993).

7.   A. Valiaev, D. W. Lim, T. G. Oas, A. Chilkoti, S. Zauscher, *J. Am. Chem. Soc.* **129**, 6491 (2007).

8.   W. E. Fowler, L. J. Fretto, K. K. Hamilton, H. P. Erickson, P. A. McKee, *J. Clin. Invest.* **76**, 1491 (1985).

9.   H. Slayter, J. Loscalzo, P. Bockenstedt, R. I. Handin, *J. Biol. Chem.* **260**, 8559 (1985).

10.   S. W. Schneider *et al.*, *Proc. Natl. Acad. Sci. U. S .A.* **104**, 7899 (2007).

11.   J. E. Sadler, *Annu. Rev. Biochem.* **67**, 395 (1998).

12.   H. Shankaran, S. Neelamegham, *Biophys. J.* **86**, 576 (Jan, 2004).

13.   F. S. Henyey, Y. Rabin, *J. Chem. Phys.* **82**, 4362 (1985, 1985).

14.   J. A. Odell, A. Keller, *J. Chem. Phys.* **88**, 4022 (1988).

15.   D. E. Smith, H. P. Babcock, S. Chu, *Science* **283**, 1724 (Mar 12, 1999).

16.   H. Lamb, *Hydrodynamics*. (Dover Publications, New York, ed. 6th, 1945).

17.   P. G. De Gennes, *Scaling Concepts in Polymer Physics*. (Cornell University Press, Ithaca and London, 1979).

18.   A. Alexander-Katz, M. F. Schneider, S. W. Schneider, A. Wixforth, R. R. Netz, *Phys. Rev. Lett.* **97**, 138101 (2006).

19.   G. B. Jeffrey, *Proc. R. Soc. Lond.* 161 (1922).

20.   Z. M. Ruggeri, G. L. Mendolicchio, *Circ. Res.* **100**, 1673 (2007).

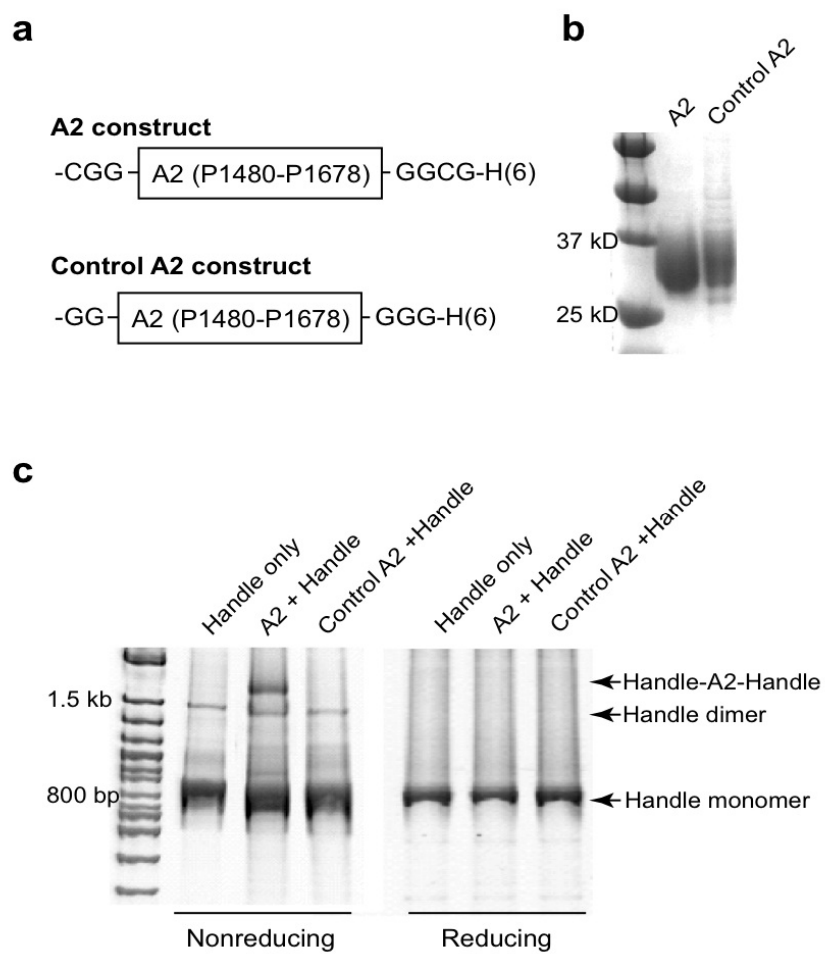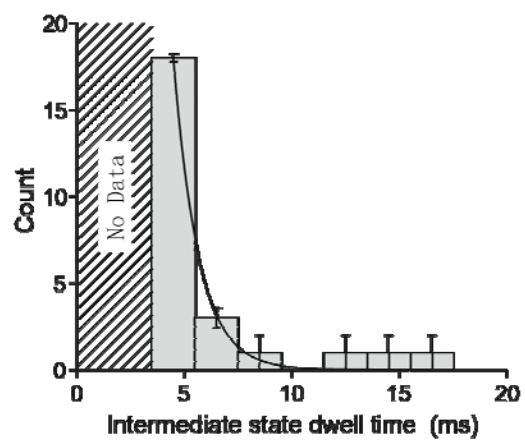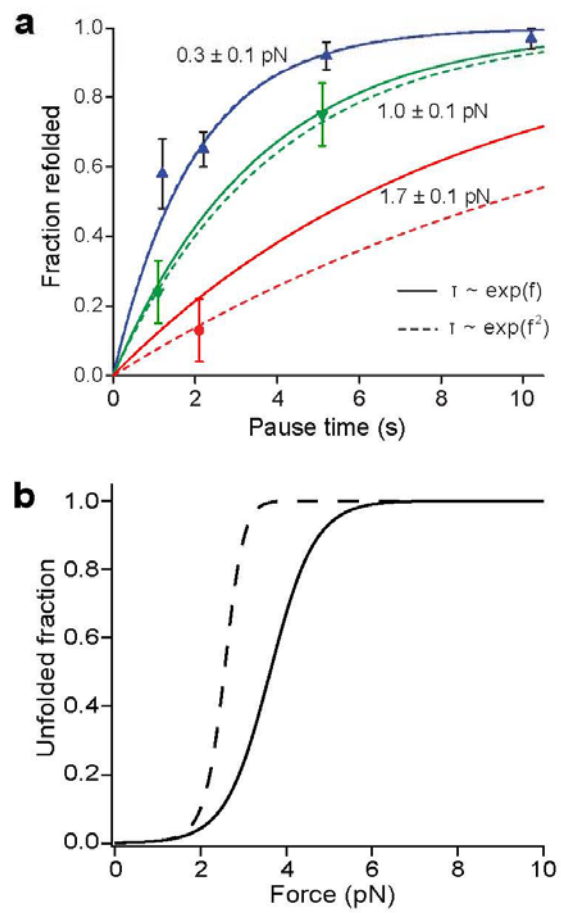21.   H. M. Tsai, *Semin. Thromb. Hemostat.* **29**, 479 (2003).

a

A2 construct

-CGG―│A2 (P1480-P1678)│―GGCG-H(6)

Control A2 construct

-GG―│A2 (P1480-P1678)│―GGG-H(6)

b

c

Fig. S1

Fig. S2

Fig. S3